

Early-stage dynamics of impact-induced hardening of dense suspensions of millimeter-sized particles

Hirokazu Maruoka^{1,2} and Hisao Hayakawa¹

¹*Yukawa Institute for Theoretical Physics, Kyoto University, Kyoto 606-8502, Japan*

²*Okinawa Institute of Science and Technology, Onna, Okinawa 904-0497, Japan **

(*hisao@yukawa.kyoto-u.ac.jp)

(*hirokazu.maruoka@oist.jp, hmaruoka1987@gmail.com)

(Dated: Thursday 18th July, 2024)

This study investigates the phenomenon of the early-stage dynamics of impact-induced hardening in dense suspensions, where materials undergo solidification upon impact. While Stokes flow theory traditionally applies to suspensions with micrometer-sized particles due to their low Reynolds numbers, suspensions containing larger particles defy such idealizations. Our work focuses on the early-stage impact-induced hardening of suspensions containing millimeter-sized particles through dynamic impact experiments. We are particularly interested in the maximum drag force F_{\max} acting on the projectile as a function of the impact speed u_0 . We successfully conducted experiments using these suspensions and confirmed the relation $F_{\max} \sim u_0^{3/2}$ for relatively large u_0 as observed in the previous studies suspensions of micrometer-sized particles. Our findings reveal that the early-stage behaviors of millimeter-sized particle suspensions align well with predictions from the floating model, typically applicable under Stokes flow conditions. This research sheds light on the complex dynamics of impact-induced hardening in dense suspensions, particularly with larger particles, advancing our understanding beyond conventional micrometer-sized systems.

I. INTRODUCTION

The investigation of impact dynamics within dense suspensions has garnered substantial interest due to its broad applicability across industrial processes and planetary sciences [1]. An intriguing phenomenon within dense suspensions is impact-induced hardening (IIH), a phenomenon enabling locomotion stop liquids while causing sinking for individuals standing or walking [2]. This behavior finds practical utility in applications such as protective vests [3]. Extensive experimental [4–9] and theoretical [10–12] studies have explored IIH, distinguishing it from discontinuous shear thickening (DST) [2, 13–15] by its localized nature versus DST's global manifestation, transient behavior versus steadiness, and distinct shear stress responses [10].

A primary focus in IIH research involves elucidating the dynamic impact experiments of projectiles [16–18], where the forces can be observed by the time evolution of projectiles based on contact mechanics [19]. Early-stage dynamics of IIH are governed initially by a viscous force [9, 11, 12], and subsequently, an elastic force plays an important role [8, 10–12]. Notably, empirical observations suggest a relationship between the maximum drag force F_{\max} and impact speed u_0 , approximated by $F_{\max} \sim u_0^{3/2}$ predicted by the "viscous model" [9] and the "floating model" [11, 12] which are equivalent models. This result is similar to the relation $F_{\max} \sim u_0^{4/3}$ observed for impact processes in dry granular materials [20, 21].

The previous theoretical studies [10–12] rely on a lattice-Boltzmann method (LBM) and discrete element method. Although their model analysis agrees with that of experimental results [9], there are various questions about the applicability of their analysis. Their approach is believed to be valid only if the suspended particles are immersed in a viscous fluid in which the Reynolds number is quite low and Stokes approximation is valid. Because of the limitation of their computer resources, their simulation contains only less than 3000 suspension particles in fluids and the radius of the projectile is only a few times larger than that of suspension particles. If suspended particles are a typical suspension such as cornstarch or potato starch, the projectile must be quite small. If we keep the size ratio between suspension particles and the projectile, we may not use the Stokes approximation.

Building upon prior investigations, this study extends our previous work by experimentally examining IIH when a steel ball impacts a dense suspension of millimeter-sized particles. Our exploration delves deeper into the mechanical response of suspension materials to sudden mechanical stimuli, uncovering the fundamental physical mechanisms driving the observed hardening phenomenon. We critically reassess the applicability of theoretical analyses utilizing the floating model and LBM within our experimental framework, particularly focusing on early-stage dynamics and the relationship between F_{\max} and u_0 . Our findings affirm that the floating model, typically valid under Stokes flow conditions, holds relevance even for dense suspensions containing millimeter-sized particles.

* Present address

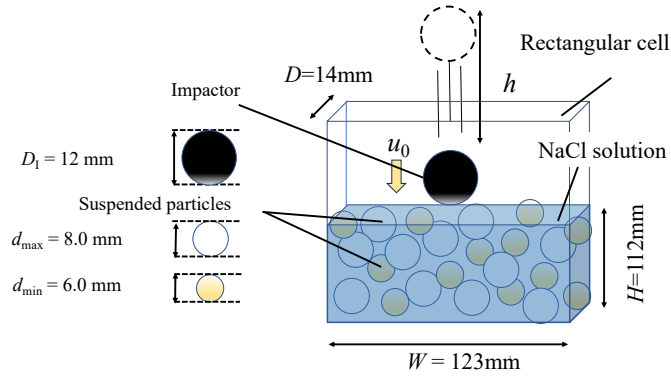


FIG. 1. An illustration of our experimental setup. We prepare a suspension containing millimeter-sized bi-disperse particles (6.0, 8.0 mm) in a solvent of NaCl solution confined in a quasi-two-dimensional rectangular container. The density of the solvent is matched with that of the particles. By dropping a metallic spherical projectile from the heights h , the projectile collides with the suspension liquid with the impact speed u_0 . We record the impact processes in a high-speed camera.

The rest of the paper is structured as follows. In the next section, we depict the experimental setup. We introduce the theoretical framework, the floating model in detail in section III. We explain the experimental results to clarify the applicability of the floating model in section IV. We conclude our results with some remarks in section V. There are three appendices, which explain the details of the buoyancy force, the exact solution of the floating model and the plots between t_{\max} and u_0 .

II. EXPERIMENT

Let us explain the setup of our experiment. We prepare a dense suspension by mixing millimeter-sized bi-disperse particles (the airsoft pellets with $d_{\max} = 8.0$ mm and 1.03 g/cm³ (MARUSHIN KOGYO CO.), the airsoft pellets with $d_{\min} = 6.0$ mm and 1.04 g/cm³ (Tokyo Marui co.)) with a NaCl solution whose the density is almost matched with that of the dispersed particles ($\rho_f \approx 1.05$ g/cm³). To observe the impact processes, the suspension is confined in a quasi-two-dimensional rectangular container (Kenis, Ltd.) with the width $W = 123$ mm, height $H = 112$ mm, and depth $D = 14$ mm. We introduce the packing fraction $\phi := V_p/V_s$ to characterize the density of N number of each particle, where $V_p := \frac{4}{3}\pi N \left[(d_{\max}/2)^2 + (d_{\min}/2)^2 \right]$ and $V_s := W \times D \times H$. We use a metallic sphere for the projectile (diameter $D_I = 12$ mm, $\rho_I = 7800$ kg · m⁻³), which was suspended by an electromagnetic (ESCO Co., Ltd., EA984CM-1) above the suspension before the impact. After switching off the magnetic force, the projectile was dropped into the suspension liquid by the impact speed u_0 . We record the impact processes with a high-speed camera (Phantom V641, Phantom T1340, Vision Research) at frame rate = 10000 fps. We control the impact velocities by varying the release height of the projectile ($h = 4 \sim 720$ mm). We perform repeated impact experiments with 10 \sim 16 times for each height to reduce specific responses of a peculiar configuration of suspended particles.

We extract the trajectories of the projectiles by optical tracking technique using the Open CV library of Python. By differentiation of the time-evolution of the position concerning time, we evaluate the time-evolution of the velocity and the acceleration of the projectile. Subtracting the buoyancy force acting on the projectile in the equation of motion of the projectile, we can evaluate the drag force acting on the projectile.

III. FLOATING MODEL

Brassard et al. [9] proposed the "viscous model", and Pradipto and Hayakawa [11, 12] proposed the "floating model" to describe the motion of the projectile in dense suspensions of micron-meter sized particles in the early stage of the impact. Later, we have recognized the equivalency of the two models. To get IIIH we need an elastic force [6–8, 10–12], which appears only in a relatively late stage of the impact process, although the floating model involves only the viscous drag force acting on the projectile except for the buoyancy force. In this paper, we adopt the floating model to describe the motion around t_{\max} at which the drag force takes F_{\max} . We depict an impact process in a suspension in Fig. 2, where the position of the bottom head of the projectile with radius a_I and its density ρ_I is denoted by z and $z = 0$ is fixed on the surface of the suspension. Thus, we are only interested in the position z satisfying $z \leq 0$, i.e, under the influence of the suspension liquid. As a result of the drag force F_D

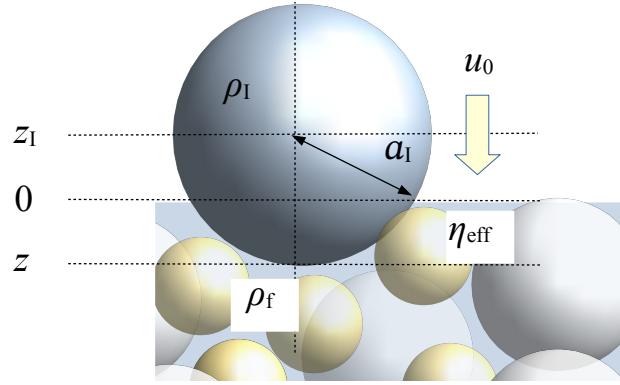


FIG. 2. An illustration of a projectile in a suspension liquid, where the impact speed is u_0 when the projectile attaches to the surface of the liquid. We denote the position of the bottom head of the projectile $z (< 0)$ where the center of mass is located at z_1 , the radius of the projectile a_1 , and the density of it is ρ_1 . The density of the solvent is ρ_f . We introduce the effective viscosity η_{eff} acting on the projectile as a mean-field viscosity of the suspension liquid in the floating model.

and buoyancy force F_B acting on the projectile, the projectile speed decreases with time and approaches zero. We should note that the maximum force F_{max} acting on the projectile appears in the relatively early stage of impact processes, and the behavior of the projectile around t_{max} can be understood without the elastic force acting on the projectile, at least, for micro-meter sized suspensions and LBM simulations [9, 11, 12].

Let us discuss the buoyancy force F_B acting on the projectile. Although F_B should be proportional to the volume inside the liquid and the gravity directly acts on the projectile in the part outside the liquid, we simply adopt an approximate expression for F_B as [11, 12]

$$F_B \simeq -m_1 g \left(1 - \frac{\rho_f}{\rho_1} \right). \quad (1)$$

where m_1 is the mass of the projectile, g is the gravitational constant, ρ_f is the density of the solvent and ρ_1 is the density of the projectile. The validity of this simplification is argued in Appendix A.

Next, we discuss the drag force F_D acting on the projectile. In the floating model, we assume that the drag force is proportional to the moving velocity because the original floating model is applied to the motion of the projectile in a Stokes fluid (see the derivation in Ref. [11]). If we assume such a model, the drag force acting on a partially filled projectile in the liquid is expressed as

$$F_D = 3\pi\eta_{\text{eff}} \frac{dz}{dt} z \quad (2)$$

where η_{eff} is an effective viscosity. For simplicity, we assume that η_{eff} is independent of u_0 but depends on ϕ . The expression of Eq. (2) is reduced to the Stokes drag force for a filled projectile in the liquid for $z \leq -2a_1$. Thus, Eq. (2) is only valid for $-2a_1 < z < 0$. It is controversial whether the drag force F_D can be used for a suspension of millimeter-sized particles because fluid flows around a large particle to generate vortices. Nevertheless, we may examine Eq. (2) for a fluid flow around a projectile in a dense suspension of millimeter-sized particles because the interstitial distance between suspended particles is too small to generate vortices. The validity of this model will be examined by the comparison between the model analysis and experimental results.

With the aid of Eqs. (1) and (2), the motion of the projectile in the early stage may be described by

$$m_1 \frac{d^2 z}{dt^2} = -m_1 g \left(1 - \frac{\rho_f}{\rho_1} \right) + 3\pi\eta_{\text{eff}} \frac{dz}{dt} z. \quad (3)$$

The dimensionless form of Eq. 3 is expressed as

$$\frac{d^2 Z}{d\tau^2} = -(1 - \xi) + \eta \frac{dZ}{d\tau} Z \quad (4)$$

where

$$Z := \frac{z}{a_1}, \quad \tau := \sqrt{\frac{g}{a_1}} t, \quad \xi := \frac{\rho_f}{\rho_1}, \quad \eta := \frac{3\pi\eta_{\text{eff}} a_1^{3/2}}{g^{1/2} m_1}, \quad U_0 := \frac{u_0}{\sqrt{a_1 g}}. \quad (5)$$

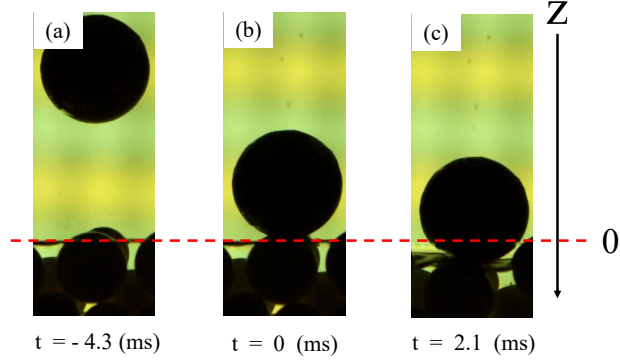


FIG. 3. A set of experimental snapshots of an impact process for $\phi = 0.56$ and $u_0 = 3.1$ m/s. Note that 2.1 ms after the first impact (the middle figure) the force acting on the projectile exhibits the maximum value F_{\max} . The movie is available at Ref.[22].

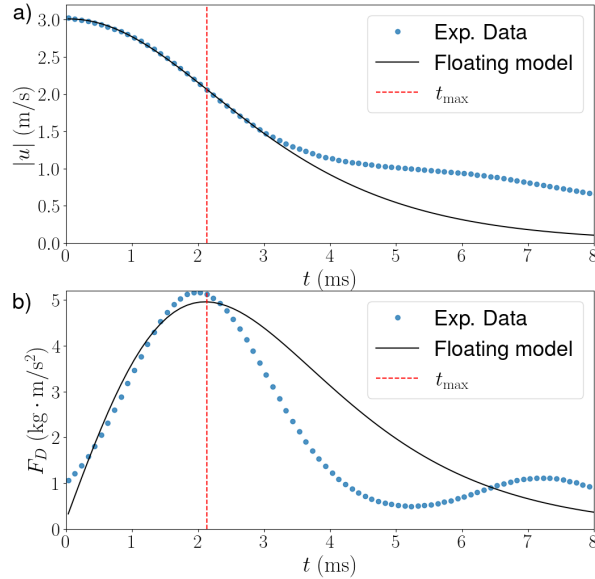


FIG. 4. The time evolution of the speed of the projectile a) and the drag force acting on the projectile b) for $\phi = 0.56$ and $u_0 = 3.1$ m/s. The blue dots are experimental data. The solid lines are the solution of the floating model Eq. (3) with a fitting parameter η . The dashed vertical red line indicates the time t_{\max} to take F_{\max} .

Equation (4), which is equivalent to Eq. (3), is the floating model [9, 11, 12].

As shown in Refs. [11, 12] and Appendix B, we can solve Eq. (4) exactly. The exact solution of Eq. (4) leads to F_{\max} , which obeys a power law in the high impact speed: [11]

$$\tilde{F}_{\max} = \frac{\sqrt{2\eta}}{3} U_0^{\frac{3}{2}} \quad (\eta U_0 \gg 1), \quad (6)$$

where $\tilde{F}_{\max} := F_{\max}/m_{\text{I}g}$.

IV. RESULTS

Let us show the experimental results and examine whether the floating model introduced in the previous section can be used in the early stage of dynamics focusing on the relationship between F_{\max} and u_0 . Figure 3 is a typical set of experimental snapshots of an impact process for $\phi = 0.56$ and $u_0 = 3.1$ m/s. Figure 3 (b) is a snapshot corresponding to the first hit of the projectile on the liquid surface at $t = 0$. Figure 3 (c) is a snapshot when the drag force acting on the projectile reaches the maximum value F_{\max} at $t_{\max} = 2.1$ ms after the first impact. The movie of the impact process is available in Ref. [22].

The projectile stops in the middle of the suspension for the dense suspensions ($\phi \geq 0.48$), where the projectile cannot sneak in the suspension liquid for low-speed impact while it can sneak in the liquid completely for high-speed impact. For low packing fractions such as $\phi = 0.40$, the projectile penetrates the liquid completely to reach the bottom of the container.

With the aid of optical tracking, we can trace the motion of the projectile. Then, we can evaluate the velocity and acceleration of the projectile as in Fig. 4. The drag force is estimated by subtracting the buoyancy force F_B from the acceleration of the projectile. As shown in Fig. 4 the projectile slows down after the impact by the drag force F_D where F_D takes the maximum value F_{\max} at t_{\max} . In this figure, the dots are obtained in the experiments, and the solid lines are the fitting curves using the solution of the floating model Eq.(3). Surprisingly, the solution of the floating model Eq. (3) with a fitting parameter $\eta := 3\pi\eta_{\text{eff}}a_1^{3/2}/(g^{1/2}m_1)$ gives reasonable agreement with the experimental results, at least, for $t < t_{\max} \approx 2.1$ ms corresponding to F_{\max} , although there is some discrepancy between the solution of the floating model and the experimental results for $t > t_{\max}$. Because we focus only on the early stage dynamics for $t \leq t_{\max}$ in this paper, we do not have to worry about the discrepancy caused by an elastic force acting on the projectile in the late stage. Thus, we can use the floating model to describe the motion of the projectile, at least, for $t \leq t_{\max}$, $u_0 = 3.1$ m/s, and $\phi = 0.56$.

Figure 5 plots of \tilde{F}_{\max} against U_0 for various packing fractions, $\phi = 0.40, 0.48, 0.51$, and 0.56 . The blue solid circles indicate experimental estimations of \tilde{F}_{\max} while the dashed lines are the numerical solutions of the floating model Eq. (4), where the dimensionless effective viscosity η is treated as a fitting parameter. From our results, all experimental data from $\phi = 0.40$ to $\phi = 0.56$ are well fitted by the solution of the floating model Eq. (4). We also confirm the asymptotic behavior $\tilde{F}_{\max} \sim U_0^{3/2}$ for $U_0 \gg 1$ as well as $t_{\max} \sim u_0^{-1/2}$ (see Appendix C) [11, 12].

Thus, we conclude that the floating model can be used even for suspensions of millimeter-sized particles for a wide range of parameters.

Figure 6 exhibits how the dimensionless effective viscosity η depends on ϕ . Although the error bars are large, this figure suggests that η is insensitive to ϕ . This is consistent with Ref. [12] where they observed only a slight increment of the effective viscosity after the impact of the projectile.

V. CONCLUDING REMARKS

In conclusion, this study establishes the applicability of the floating model [9, 11, 12] across suspensions containing millimeter-sized particles, particularly in describing the relationship between F_{\max} and u_0 satisfying $F_{\max} \sim u_0^{3/2}$ for $u_0 \gg \sqrt{ga_1}$ as evidenced by our experimental findings. Our results affirm the validity of previous lattice Boltzmann method (LBM) simulations [11, 12] involving sparse particle suspensions, despite the disparity in size ratio between the projectile and suspended particles.

Interestingly, our findings challenge conventional understanding, suggesting that Stokes flow may indeed describe fluid interactions around large particles under certain conditions. We may propose that this validation of the floating model could stem from scenarios where dense suspensions near jamming points exhibit unexpectedly high effective viscosities[23], though our data in Fig. 6 suggests otherwise for little volume fraction ϕ dependence of η . Alternatively, a plausible explanation involves the suppression of vortices due to neighboring particles in dense suspensions, akin to concepts in turbulence drag reduction using polymers and suspended particles as Refs. [24, 25].

Looking ahead, elucidating the reasons behind the applicability of the floating model in millimeter-sized particle suspensions remains a critical future research objective. While this paper primarily explores early-stage dynamics, future studies should further investigate the role of elastic forces highlighted in previous experiments [8] and theoretical works [11, 12] during the later stages of impact-induced hydrodynamic interactions.

VI. ACKNOWLEDGMENT

We thank the useful comments by Frédéric van Wijland, and Pradipto. HM thanks Mahesh Bandi, and members of the Non-equilibrium Physics Unit at OIST, and Yutaro Motoori for their useful advice and comments. This work is partially supported

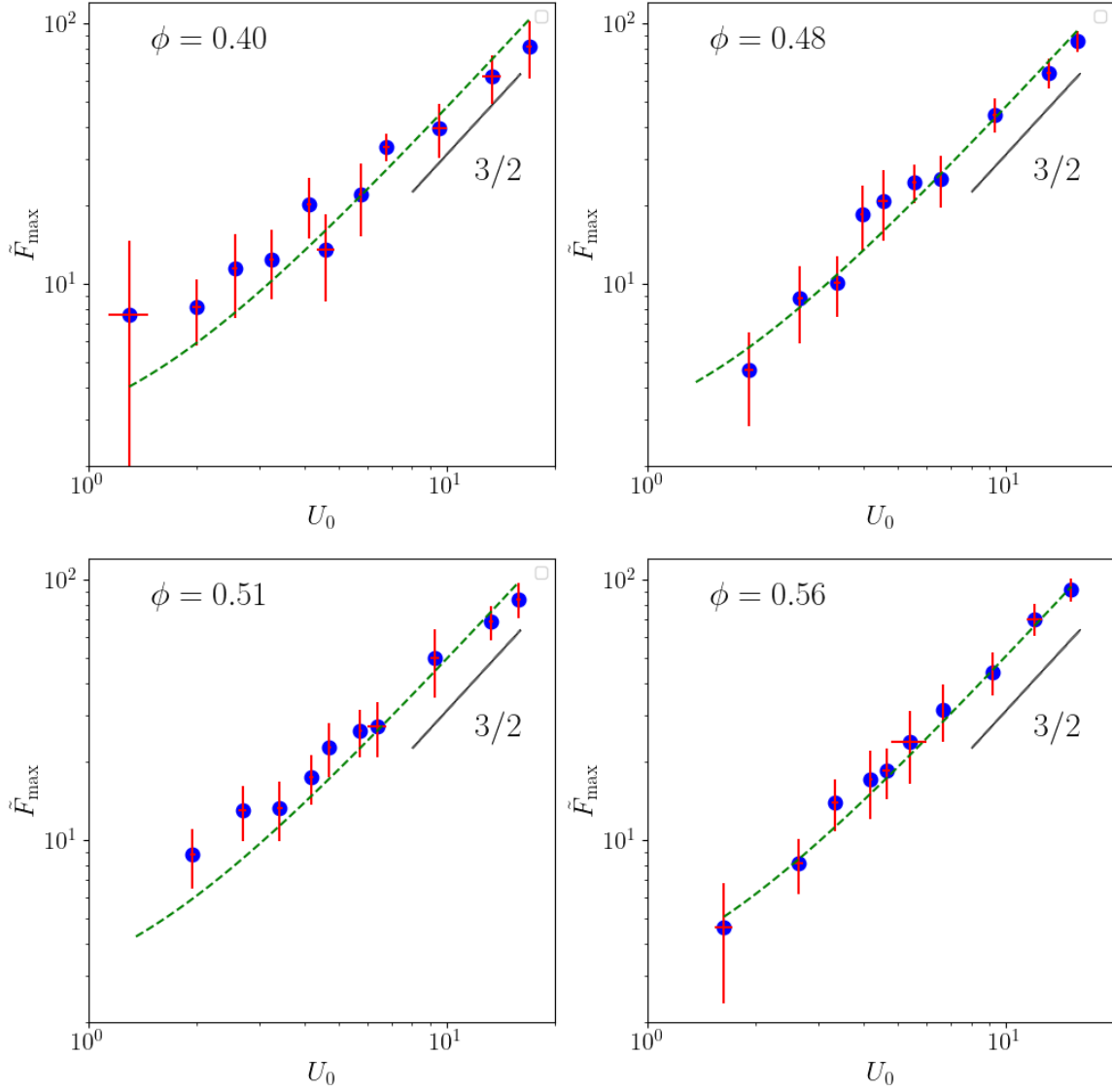


FIG. 5. The plots between the dimensionless maximum force $\tilde{F}_{\max} := F_{\max}/m_1g$ and impact-speed $U_0 := u_0/\sqrt{a_1g}$ for various packing fractions $\phi = 0.40, 0.48, 0.51$, and 0.56 . The blue solid circles indicate the experimental results and the dashed lines are obtained by the numerical solutions of the floating model Eq. (4). The black solid lines are the guide lines $\tilde{F}_{\max} \propto U_0^{3/2}$ as expected from Eq. (6).

by Grants-in-Aid of MEXT, Japan for Scientific Research, Grant Nos. JP21H01006 and JP24K17022, and the Kyoto University Foundation.

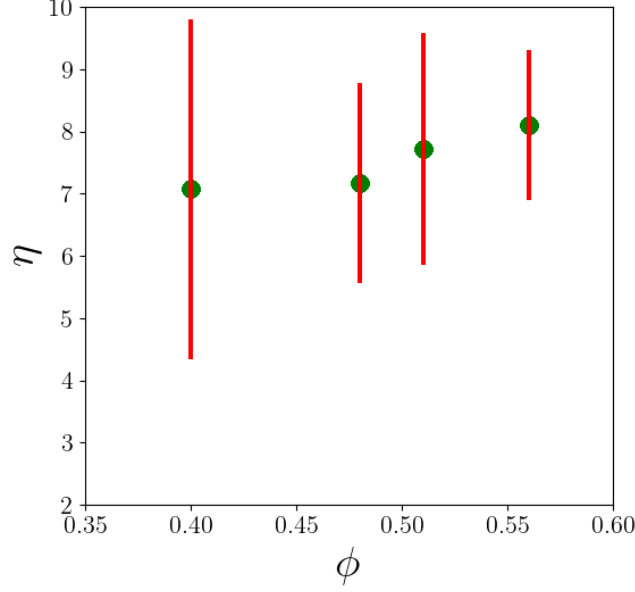


FIG. 6. Plot of the effective viscosity $\eta := 3\pi\eta_{\text{eff}}a_1^{3/2}/(g^{1/2}m_1)$ against ϕ . The red vertical lines express error bars of the estimated η .

Appendix A: The expression of the buoyancy force

If a projectile with the density ρ_1 is located in a fluid with density $\rho_f (\neq \rho_1)$, the motion of the projectile is affected by the buoyancy force. The expression of the buoyancy force must depend on the immersed volume of the projectile in the fluid, where the immersed volume $V(z)$ of the projectile at the location z (see Fig. 2 in the main text) is expressed as

$$\begin{aligned} V(z) &= \int_0^z \pi a_1'^2 dz' \\ &= \frac{\pi a_1^3}{3} \left[3 \left(\frac{z}{a_1} \right)^2 - \left(\frac{|z|}{a_1} \right)^3 \right]. \end{aligned} \quad (\text{A1})$$

This expression is valid for $-2a_1 \leq z \leq 0$.

Thus, the buoyancy force is given by

$$\begin{aligned} F_B &= -g\{\rho_1 V_1 - \rho_f V(z)\} \\ &= -m_1 g \left\{ 1 - \frac{\rho_f}{4\rho_1} \left[3 \left(\frac{z}{a_1} \right)^2 - \left(\frac{|z|}{a_1} \right)^3 \right] \right\} \end{aligned} \quad (\text{A2})$$

where ρ_f is the density of fluid and ρ_1 is the density of the projectile. Once we adopt Eq. (A2), we cannot solve the floating model exactly. Fortunately, if we assume $\rho_1 \gg \rho_f$, the simplified buoyancy force Eq. (1) as in Refs. [11, 12] gives the reasonable agreement with that in Eq. (A2) as shown in Fig. 7 a). The error caused by the approximation Z_{Apx} in Eq. (1) plots $|Z_{\text{Ext}} - Z_{\text{Apx}}|/|Z_{\text{Ext}}|$ in Fig. 7 b), where Z_{Ext} is the solution of the floating model (4) with Eq. (A2). As shown in this figure, the error by the simplified expression in Eq. (1) is less than 0.8%. Thus, for simplicity, we adopt Eq. (1) for the buoyancy force in this paper.

Appendix B: Exact solution of floating model

As shown in Refs. [11, 12], the floating model Eq. (4) with Eq. (1) can be solved exactly. The explicit expression of $Z(\tau)$ is given by

$$Z(\tau) = - \left[\frac{4(1-\xi)}{\eta^2} \right]^{1/3} \frac{-\text{Ai}'(\Xi)\text{Bi}'(\Lambda) + \text{Ai}'(\Lambda)\text{Bi}'(\Xi)}{\text{Ai}'(\Lambda)\text{Bi}(\Xi) + \text{Ai}(\Xi)\text{Bi}'(\Lambda)}, \quad (\text{B1})$$

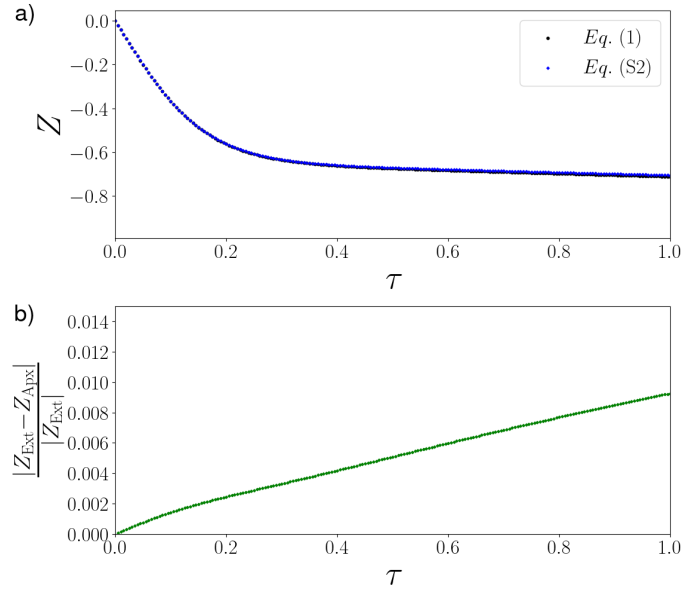


FIG. 7. Comparison between the numerical solutions of the exact expression of the buoyancy force Eq. (A2) and the approximate expression Eq. (1), where we plot the time evolution of position a) and their difference of two expressions b).

where $\Xi := \left(\frac{\eta(1-\xi)}{2}\right)^{1/3} \left(\tau + \frac{U_0}{1-\xi}\right)$, $\Lambda := \left(\frac{\eta}{2(1-\xi)^2}\right)^{1/3} U_0$. $\text{Ai}(x)$ and $\text{Bi}(x)$ are Airy functions as $\text{Ai}(x) := \frac{1}{\pi} \int_0^\infty \cos\left(\frac{t^3}{3} + xt\right) dt$, and $\text{Bi}(x) := \frac{1}{\pi} \int_0^\infty \left[e^{-\frac{t^3}{3} + xt} + \sin\left(\frac{t^3}{3} + xt\right)\right] dt$, $\text{Ai}'(x)$ and $\text{Bi}'(x)$ are their derivatives with respect to x , respectively. Note that F_{\max} cannot be obtained exactly, although the asymptotic expression for $U_0 \gg 1$ can be evaluated [11].

Appendix C: t_{\max} versus the impact speed u_0

Figure 8 presents the result for t_{\max} versus u_0 . Although the data has large error bars, the result seems to be consistent with the previously reported result, $t_{\max} \sim u_0^{-1/2}$ for $u_0 \gg \sqrt{g\alpha l}$ [9, 11].

-
- [1] H. Katsuragi, *Physics of Soft Impact and Cratering* (Springer, Berlin, 2016).
 - [2] E. Brown and H. M. Jaeger, Shear thickening in concentrated suspensions: Phenomenology, mechanisms and relations to jamming, *Rep. Prog. Phys.* **77**, 046602 (2014).
 - [3] Y. S. Lee, E. D. Wetzels, and N. J. Wagner, The ballistic impact characteristics of Kevlar woven fabrics impregnated with a colloidal shear thickening fluid, *J. Mater. Sci.* **38**, 2825 (2003).
 - [4] S. R. Waitukaitis and H. M. Jaeger, Impact-activated solidification of dense suspensions via dynamic jamming fronts, *Nature (London)* **487**, 205 (2012).
 - [5] E. Han, I. R. Peters, and H. M. Jaeger, High-speed ultrasound imaging in dense suspensions reveals impact-activated solidification due to dynamic shear jamming, *Nat. Commun.* **7**, 12243 (2016).
 - [6] M. Roche, E. Myftiu, M. C. Johnston, P. Kim, and H. A. Stone, Dynamic Fracture of Nonglassy Suspensions, *Phys. Rev. Lett.* **110**, 148304 (2013).
 - [7] R. Maharjan, S. Mukhopadhyay, B. Allen, T. Storz, and E. Brown, Constitutive relation for the system-spanning dynamically jammed region in response to impact of cornstarch and water suspensions, *Phys. Rev. E* **97**, 052602 (2018).
 - [8] K. Egawa and H. Katsuragi, Bouncing of a projectile impacting a dense potato-starch suspension layer, *Phys. Fluids* **31**, 053304 (2019).
 - [9] M. Brassard, N. Causley, N. Krizou, J. A. Dijkman, and A. H. Clark, Viscous-like forces control the impact response of shearthickening dense suspensions, *J. Fluid Mech.* **923**, A38 (2021).
 - [10] Pradipto and H. Hayakawa, Impact-induced hardening in dense frictional suspensions, *Phys. Rev. Fluids* **6**, 033301 (2021).
 - [11] Pradipto and H. Hayakawa, Viscoelastic response of impact process on dense suspensions, *Phys. Fluids* **33**, 093110 (2021).
 - [12] Pradipto and H. Hayakawa, Effective viscosity and elasticity in dense suspensions under impact: Toward a modeling of walking on suspensions, *Phys. Rev. E* **108**, 024604 (2023).

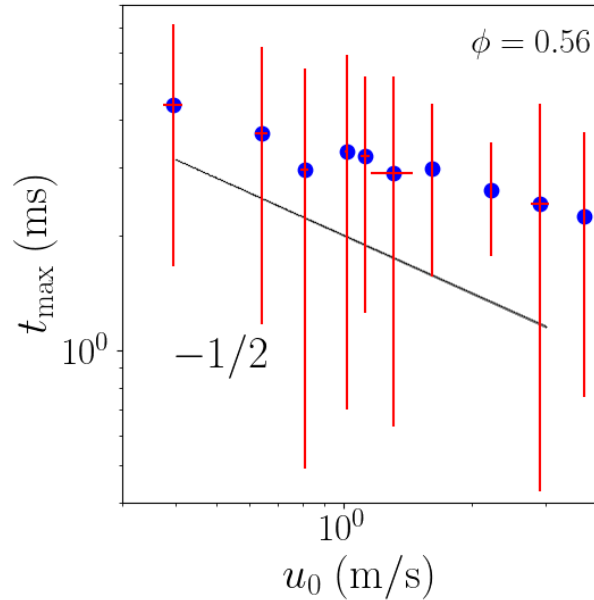


FIG. 8. The plots between t_{\max} and their impact-velocities u_0 .

- [13] M. Otsuki and H. Hayakawa, Critical scaling near jamming transition for frictional granular particles, *Phys. Rev. E* **83**, 051301 (2011).
- [14] R. Seto, R. Mari, J. F Morris, and M. M. Denn, Discontinuous shear thickening of frictional hard-sphere suspensions, *Phys. Rev. Lett.* **111**, 218301 (2013)
- [15] C. Ness, R. Seto, and R. Mari, The physics of dense suspensions, *Annu. Rev. Condens. Matter Phys.* **13**, 97 (2022).
- [16] E. Falcon, C. Laproche, S. Fauve, C. Coste, Behavior of one inelastic ball bouncing repeatedly off the ground, *Eur. Phys. J. B* **3**, 45 (1998).
- [17] T. Chastel, P. Gondret, A. Mongruel, Texture-driven elasto-hydrodynamic bouncing, *J. Fluid Mech.* **805**, 577 (2016).
- [18] H. Maruoka, A framework for crossover of scaling law as a self-similar solution: dynamical impact of viscoelastic board, *Eur. Phys. J. E* **46**, 35 (2023).
- [19] K.L. Johnson, *Contact Mechanics* (Cambridge University Press, Cambridge, 1985).
- [20] N. Krizou and A. H. Clark, Power-Law Scaling of Early-Stage Forces during Granular Impact, *Phys. Rev. Lett.* **124**, 178002 (2020).
- [21] M. K. Mandal, and S. Roy, High speed impact on granular media: breakdown of conventional inertial drag models *Soft Matter*, **20**, 877 (2024).
- [22] See Supplemental Material for a movie of the impact process for $\phi = 0.56$ and $u_0 = 3.1$ m/s in the frame rate for 10000 fps.
- [23] É. Guazzelli, O. Pouliquen, Rheology of dense granular suspensions, *J. Fluid Mech.* **852** (2018).
- [24] P. G. de Gennes, Towards a scaling theory of drag reduction, *Physica A* **140**, 9 (1986).
- [25] H. Dave and M. H. Kasbaoui, Mechanisms of drag reduction by semidilute inertial particles in turbulent channel flow *Phys. Rev. Fluids*, **8**, 084305 (2023).